To catch and reverse a quantum jump mid-flight

Z. K. Minev[1,5]*, S. O. Mundhada[1], S. Shankar[1], P. Reinhold[1], R. Gutiérrez-Jáuregui[2], R. J. Schoelkopf[1], M. Mirrahimi[3,4], H. J. Carmichael[2] & M. H. Devoret[1]*

In quantum physics, measurements can fundamentally yield discrete and random results. Emblematic of this feature is Bohr's 1913 proposal of quantum jumps between two discrete energy levels of an atom[1]. Experimentally, quantum jumps were first observed in an atomic ion driven by a weak deterministic force while under strong continuous energy measurement[2–4]. The times at which the discontinuous jump transitions occur are reputed to be fundamentally unpredictable. Despite the non-deterministic character of quantum physics, is it possible to know if a quantum jump is about to occur? Here we answer this question affirmatively: we experimentally demonstrate that the jump from the ground state to an excited state of a superconducting artificial three-level atom can be tracked as it follows a predictable 'flight', by monitoring the population of an auxiliary energy level coupled to the ground state. The experimental results demonstrate that the evolution of each completed jump is continuous, coherent and deterministic. We exploit these features, using real-time monitoring and feedback, to catch and reverse quantum jumps mid-flight—thus deterministically preventing their completion. Our findings, which agree with theoretical predictions essentially without adjustable parameters, support the modern quantum trajectory theory[5–9] and should provide new ground for the exploration of real-time intervention techniques in the control of quantum systems, such as the early detection of error syndromes in quantum error correction.

Bohr conceived of quantum jumps[1] in 1913, and whereas Einstein elevated the hypothesis to the level of a quantitative rule with his AB coefficient theory[10,11], Schrödinger strongly objected to their existence[12]. The nature and existence of quantum jumps remained controversial for seven decades until they were directly observed in a single system[2–4]. Since then, quantum jumps have been observed in various atomic[13–16] and solid-state[17–21] systems. Recently, they have been recognized as an essential phenomenon in quantum feedback control[22,23], and in particular, for detecting and correcting decoherence-induced errors in quantum information systems[24,25].

Here, we focus on the canonical case of quantum jumps between two levels indirectly monitored by a third—the case that corresponds to the original observation of quantum jumps in atomic physics[2–4] (see the level diagram of Fig. 1a). A surprising prediction emerges according to quantum trajectory theory[5,26–28]: not only does the state of the system evolve continuously during the jump between the ground $|G\rangle$ and excited $|D\rangle$ state, but it is predicted that there is always a latency period prior to the jump, during which it is possible to acquire a signal that warns of the imminent occurrence of the jump (see Supplementary Information section IIA). This advance warning signal consists of a rare, particular lull in the excitation of the ancilla (bright) state $|B\rangle$. The acquisition of this signal requires the time-resolved, fully efficient detection of every de-excitation of $|B\rangle$. Exploiting the specific advantages of superconducting artificial atoms and their quantum-limited readout chain, we designed an experiment that implements with maximum fidelity and minimum delay the detection of the advance warning signal occurring before the quantum jump (see rest of Fig. 1).

First, we developed a superconducting artificial atom with the necessary V-shaped level structure (see Fig. 1a and Methods). It consists, besides the ground level $|G\rangle$, of one protected, dark level $|D\rangle$—engineered to couple only minimally to any dissipative environment or any measurement apparatus—and one ancilla level $|B\rangle$, whose occupation is monitored at rate Γ. Quantum jumps between $|G\rangle$ and $|D\rangle$ are induced by a weak Rabi drive Ω_{DG}—although this drive can eventually be turned off during the jump, as explained later. Because a direct measurement of the dark level is not feasible nor desired, the jumps are monitored using the Dehmelt shelving scheme[2]. Thus, the occupation of $|G\rangle$ is linked to that of $|B\rangle$ by the strong Rabi drive Ω_{BG} ($\Omega_{DG} \ll \Omega_{BG} \ll \Gamma$). In the atomic physics shelving scheme[2–4], an excitation to $|B\rangle$ is recorded by detecting the emitted photons from $|B\rangle$ with a photodetector. From the detection events—referred to in the following as 'clicks'—one infers the occupation of $|G\rangle$. On the other hand, from the prolonged absence of clicks (to be defined precisely below; see also Supplementary Information section II), one infers that a quantum jump from $|G\rangle$ to $|D\rangle$ has occurred. Owing to the poor collection efficiency and the dead time of photon counters in atomic physics[29], it is exceedingly difficult to detect every individual click required to faithfully register the origin in time of the advance warning signal. However, superconducting systems present the advantage of high collection efficiencies[30–32], as their microwave photons are emitted into one-dimensional waveguides and are detected with the same detection efficiencies as optical photons. Furthermore, rather than monitoring the direct fluorescence of the $|B\rangle$ state, we monitor its occupation by dispersively coupling it to an ancilla readout cavity. This further improves the fidelity of the detection of the de-excitation from $|B\rangle$ (effective collection efficiency of photons emitted from $|B\rangle$).

The readout cavity, schematically depicted in Fig. 1a by an LC circuit, is resonant at $\omega_C = 8{,}979.64$ MHz and cooled to 15 mK. Its dispersive coupling to the atom results in a conditional shift of its resonance frequency by $\chi_B/2\pi = -5.08 \pm 0.2$ MHz when the atom is in $|B\rangle$ and $\chi_D/2\pi = -0.33 \pm 0.08$ MHz when the atom is in $|D\rangle$ (see Fig. 1c). The engineered large asymmetry between χ_B and χ_D together with the cavity coupling rate to the output waveguide, $\kappa/2\pi = 3.62 \pm 0.05$ MHz, renders the cavity response markedly resolving for $|B\rangle$ versus not-$|B\rangle$, yet non-resolving[30] for $|G\rangle$ versus $|D\rangle$, thus preventing information about the dark transition from reaching the environment. When probing the cavity response at $\omega_C - \chi_B$, the cavity either remains empty, when the atom is in $|G\rangle$ or $|D\rangle$, or fills with $\bar{n} = 5 \pm 0.2$ photons when the atom is in $|B\rangle$. This readout scheme yields a transduction of the $|B\rangle$-occupancy signal with fivefold amplification, which is an important advantage to overcome the noise of the following amplification stages. To summarize, in this readout scheme, the cavity probe inquires: is the atom in $|B\rangle$ or not? The time needed to arrive at an answer with a confidence level of 68% (signal-to-noise ratio of 1) is $\Gamma^{-1} \approx 1/(\kappa\bar{n}) = 8.8$ ns for an ideal cavity-amplifier chain (Supplementary Information section IIIC).

Importantly, the engineered near-zero coupling between the cavity and the $|D\rangle$ state protects the $|D\rangle$ state from harmful effects, including Purcell relaxation, photon shot-noise dephasing and the as-yet
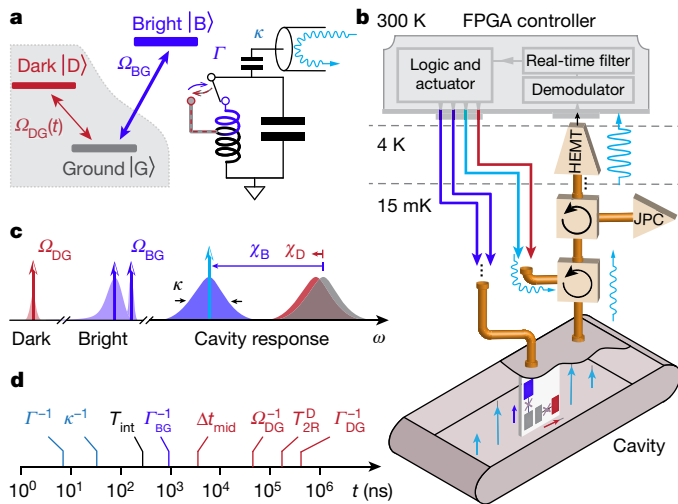
Fig. 1 | Principle of the experiment. a, Three-level atom possessing a hidden transition (shaded region) between its ground $|G\rangle$ and dark $|D\rangle$ state, driven by the Rabi drive $\Omega_{DG}(t)$. Quantum jumps between $|G\rangle$ and $|D\rangle$ are indirectly monitored by a stronger Rabi drive Ω_{BG} between $|G\rangle$ and the bright state $|B\rangle$, whose occupancy is continuously monitored at rate Γ by an auxiliary oscillator (LC circuit on the right), itself measured in reflection by continuous-wave microwave light (depicted in light blue). When the atom is in $|B\rangle$, the resonance frequency of the LC circuit shifts to a lower frequency than when the atom is in $|G\rangle$ or $|D\rangle$ (effect schematically represented by switch). Therefore, the probe tone performs a $|B\rangle$/not-$|B\rangle$ measurement on the atom and is blind to any superposition of $|G\rangle$ and $|D\rangle$. **b**, The actual atom and LC oscillator used in the experiment comprise a superconducting circuit consisting of two strongly hybridized transmon qubits, fabricated on a chip (white rectangle), placed inside a readout resonator cavity at 15 mK. Each transmon consists of two metal rectangular pads connected by a wire interrupted by the Josephson tunnel junction, whose location is indicated by a cross. Control signals for the atom and cavity are supplied by the FPGA controller. This fast electronics system monitors the reflected signal from the cavity and, after demodulation and filtering, actuates the control signals. The amplifier chain includes circulators (curved arrows) and amplifiers (triangles and trapezoids). HEMT, high-electron-mobility transistor; JPC, Josephson parametric converter. **c**, Frequency landscape of atom and cavity responses, overlaid with the control tones shown as vertical arrows. The cavity pull χ of the atom is nearly identical for $|G\rangle$ and $|D\rangle$, but markedly distinct for $|B\rangle$. The BG drive is bi-chromatic in order to address the bright transition independently of the cavity state. **d**, Hierarchy of timescales involved in the experiment, which are required to span at least five orders of magnitude. Symbols are explained in the text and summarized in Extended Data Table 2.

essentially unexplained residual measurement-induced relaxation in superconducting qubits (Supplementary Information section I). We have measured the following coherence times for the $|D\rangle$ state:

energy relaxation $T_1^D = 116 \pm 5\,\mu s$, Ramsey coherence $T_{2R}^D = 120 \pm 5\,\mu s$ and Hahn echo $T_{2E}^D = 162 \pm 6\,\mu s$. While protected, the $|D\rangle$ state is indirectly read out in a quantum-non-demolition (QND) fashion by the combination of the V-structure, the drive between $|G\rangle$ and $|B\rangle$ and the fast $|B\rangle$-state monitoring. In practice, we can access the population of $|D\rangle$ using an 80-ns unitary rotation followed by a projective measurement of $|B\rangle$ (see Methods).

Once the state of the readout cavity is imprinted with information about the occupation of $|B\rangle$, photons leak through the cavity output port into a superconducting waveguide, which is connected to the amplification chain (see Fig. 1b), where they are amplified by a factor of 10^{12}. The first stage of amplification is a quantum-limited Josephson parametric converter, which is followed by a high-electron-mobility transistor amplifier at 4 K. The overall efficiency of the amplification chain is $\eta = 0.33 \pm 0.03$, which includes all possible loss of information, such as due to photon loss, thermal photons or jitter (see Methods). At room temperature, the heterodyne signal is demodulated by a home-built field-programmable gate array (FPGA) controller, with a 4-ns clock period for logic operations. The measurement record consists of a time series of two quadrature outcomes, I_{rec} and Q_{rec}, every 260 ns, which is the integration time T_{int}, from which the FPGA controller estimates the state of the atom in real time. To reduce the influence of noise, the controller applies a real-time, hysteretic IQ filter (see Methods), and then, from the estimated atom state, the control drives of the atom and readout cavity are actuated, realizing feedback control.

Having described the set-up of the experiment, we proceed to report its results. The field reflected out of the cavity is monitored in a free-running protocol, for which the atom is subject to the continuous Rabi drives Ω_{BG} and Ω_{DG}, as depicted in Fig. 1. Figure 2a shows a typical trace of the measurement record, displaying the quantum jumps of our three-level artificial atom. For most of the displayed duration of the record, I_{rec} switches rapidly between a low and high value, corresponding to approximately zero ($|G\rangle$ or $|D\rangle$) and five ($|B\rangle$) photons in the cavity, respectively. Spikes in Q_{rec}, such as the one at $t = 210\,\mu s$, are recognized by the FPGA logic as a short-lived excursion of the atom to a higher excited state (see Methods). The corresponding most likely state of the atom, estimated by the FPGA controller, is depicted by the colour of the dots. A change from $|B\rangle$ to not-$|B\rangle$ is equivalent to a 'click' event, in that it corresponds to the emission of a photon from $|B\rangle$ to $|G\rangle$, whose occurrence time is shown by the vertical arrows in the inferred record $dN(t)$ (top). We could also indicate upward transitions from $|G\rangle$ to $|B\rangle$, corresponding to photon absorption events (not emphasized here), which would not be detectable in the atomic case.

In the example record, the detection of clicks stops completely at $t = 45\,\mu s$, which reveals a quantum jump from $|G\rangle$ to $|D\rangle$ (see Methods for operational definition of quantum jumps). The state $|D\rangle$ survives for 90 μs before the atom returns to $|G\rangle$ at $t = 135\,\mu s$, when the rapid switching between $|G\rangle$ and $|B\rangle$ resumes until a second quantum jump to the dark state occurs at $t = 350\,\mu s$. Thus, the record presents jumps
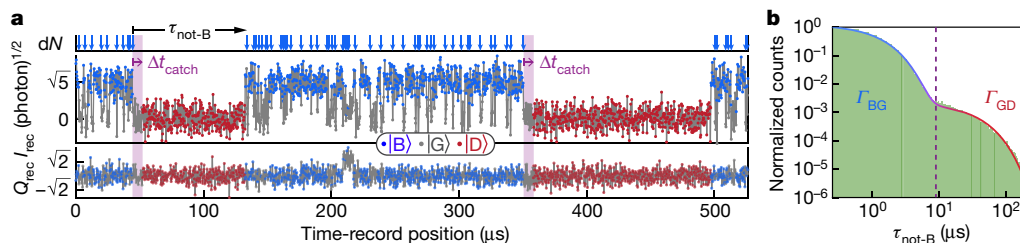
Fig. 2 | Unconditioned monitoring of quantum jumps in the three-level system. a, Typical measurement of integrated, with duration T_{int}, quadratures I_{rec} and Q_{rec} of signal reflected from readout cavity as a function of time. The colour of the dots (see key) denotes the state of the atom estimated by a real-time filter implemented with the FPGAs (see Methods). On top, the vertical arrows indicate click events (dN) corresponding to the inferred state changing from $|B\rangle$ to not-$|B\rangle$. The symbol $\tau_{\text{not-B}}$ corresponds to the time spent in not-$|B\rangle$, which is the time

between two clicks minus the last duration spent in $|B\rangle$. An advance warning that a jump to $|D\rangle$ is occurring is triggered when no click has been observed for a duration Δt_{catch}, which is chosen between 1 μs and 12 μs at the start of the experiment. **b**, Plot (log–log) of the histogram of $\tau_{\text{not-B}}$ (shaded green) for 3.2 s of continuous data of the type of **a**. Solid line is a bi-exponential fit defining jump rates $\Gamma_{BG} = (0.99 \pm 0.06\,\mu s)^{-1}$ and $\Gamma_{GD} = (30.8 \pm 0.4\,\mu s)^{-1}$.

from $|G\rangle$ to $|D\rangle$ in the form of click interruptions. These 'outer' jumps occur on a much longer timescale than the 'inner' jumps from $|G\rangle$ to $|B\rangle$.

In Fig. 2b, which is based on the continuous tracking of the quantum jumps for 3.2 s, a histogram of the time spent in not-$|B\rangle$, $\tau_{\text{not-B}}$, is shown (see Extended Data Fig. 1 for the time spent in $|B\rangle$). The panel further shows a fit of the histogram by a bi-exponential curve that models two interleaved Poisson processes. This yields the average time the atom rests in $|G\rangle$ before an excitation to $|B\rangle$, $\Gamma_{\text{BG}}^{-1} = 0.99 \pm 0.06\,\mu\text{s}$, and the average time the atom stays up in $|D\rangle$ before returning to $|G\rangle$ and being detected, $\Gamma_{\text{GD}}^{-1} = 30.8 \pm 0.4\,\mu\text{s}$. The average time between two consecutive $|G\rangle$ to $|D\rangle$ jumps is $\Gamma_{\text{DG}}^{-1} = 220 \pm 5\,\mu\text{s}$. The corresponding rates depend on the atom drive amplitudes (Ω_{DG} and Ω_{BG}) and the measurement rate Γ (Supplementary Information section II). Crucially, all the rates in the system must be distributed over a minimum of five orders of magnitude, as shown in Fig. 1d.

Having observed the quantum jumps from $|G\rangle$ to $|D\rangle$ in the free-running protocol, we proceed to conditionally actuate the system control tones to tomographically reconstruct their time dynamics (see Fig. 3a). Like in the previous case, after initiating the atom in $|B\rangle$, the FPGA controller continuously subjects the system to the atom drives (Ω_{BG} and Ω_{DG}) and to the readout tone (R). However, in the event that the controller detects a single click followed by the complete absence of clicks for a total time Δt_{catch}, the controller suspends all system drives, thus freezing the system evolution, and performs tomography, as explained in Methods. Note that in each realization, the tomography measurement yields a single $+1$ or -1 outcome, one bit of information for a single component of the density matrix. We also introduce a division of the duration Δt_{catch} into two phases, one lasting Δt_{on} during which Ω_{DG} is left on, and one lasting $\Delta t_{\text{off}} = \Delta t_{\text{catch}} - \Delta t_{\text{on}}$ during which Ω_{DG} is turned off. As we explain below, this has the purpose of demonstrating that the evolution of the jump is not simply due to the Rabi drive between $|G\rangle$ and $|D\rangle$.

In Fig. 3b, we show the dynamics of the jump mapped out in the full presence of the Rabi drive, Ω_{GD}, by setting $\Delta t_{\text{off}} = 0$. From 3.4×10^6 experimental realizations we reconstruct, as a function of Δt_{catch}, the quantum state, and present the evolution of the jump from $|G\rangle$ to $|D\rangle$ as the normalized, conditional GD tomogram (Methods). For $\Delta t_{\text{catch}} < 2\,\mu\text{s}$, the atom is predominantly detected in $|G\rangle$ (Bloch coordinate $Z_{\text{GD}} = -1$; see Methods), whereas for $\Delta t_{\text{catch}} > 10\,\mu\text{s}$ it is predominantly detected in $|D\rangle$ ($Z_{\text{GD}} = +1$). Imperfections, mostly excitations to higher levels, reduce the maximum observed value to $Z_{\text{GD}} = +0.9$ (Supplementary Information section IIIB2).

For intermediate no-click times, between $\Delta t_{\text{catch}} = 2\,\mu\text{s}$ and $\Delta t_{\text{catch}} = 10\,\mu\text{s}$, the state of the atom evolves continuously and coherently from $|G\rangle$ to $|D\rangle$—the flight of the quantum jump. The time of mid flight, $\Delta t_{\text{mid}} \equiv 3.95\,\mu\text{s}$, is markedly shorter than the Rabi period $2\pi/\Omega_{\text{DG}} = 50\,\mu\text{s}$ and is given by the function $\Delta t_{\text{mid}} = \left(\frac{\Omega_{\text{BG}}^2}{2\Gamma}\right)^{-1} \ln\left(\frac{\Omega_{\text{BG}}^2}{\Omega_{\text{DG}}\Gamma} + 1\right)$, in which Ω_{DG} enters logarithmically (Supplementary Information section IIA). The maximum coherence of the superposition, corresponding to $\sqrt{X_{\text{GD}}^2 + Y_{\text{GD}}^2}$, during the flight is 0.71 ± 0.005 (see also Extended Data Fig. 2), quantitatively understood to be limited by several small imperfections (Supplementary Information section IIIB2).

Motivated by the quantum trajectory analysis, we fit the experimental data with $Z_{\text{GD}}(\Delta t_{\text{catch}}) = a + b\tanh(\Delta t_{\text{catch}}/\tau + c)$, $X_{\text{GD}}(\Delta t_{\text{catch}}) = a' + b'\text{sech}(\Delta t_{\text{catch}}/\tau' + c')$ and $Y_{\text{GD}}(\Delta t_{\text{catch}}) = 0$. We compare the fitted jump parameters ($a, a', b, b', c, c', \tau, \tau'$) to those calculated from the theory and numerical simulations using independently measured system characteristics, and find agreement at the per cent level (Supplementary Information section IIIA).

By repeating the experiment with $\Delta t_{\text{on}} = 2\,\mu\text{s}$, in Fig. 3c, we show that the jump proceeds even if the GD drive is shut off at the beginning of the no-click period. The jump remains coherent and only differs from the previous case in a minor renormalization of the overall amplitude and timescale. The mid-flight time of the jump, $\Delta t'_{\text{mid}}$, is given by
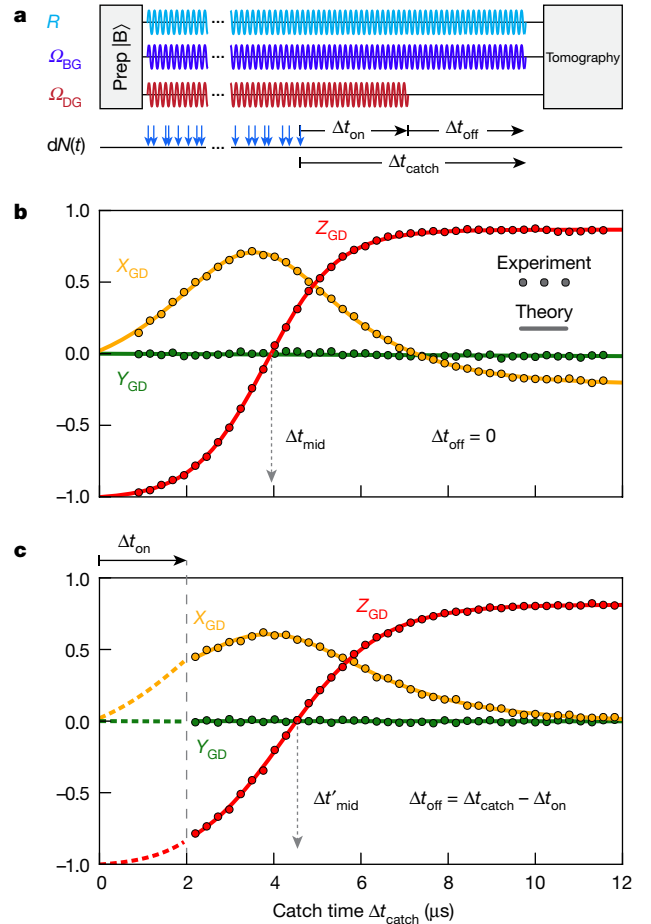
Fig. 3 | Catching the quantum jump mid-flight. a, The atom is initially prepared in $|B\rangle$. The readout tone (R) and atom Rabi drive Ω_{BG} are turned on until the catch condition is fulfilled, consisting of the detection of a click followed by the absence of click detections for a total time Δt_{catch}. The Rabi drive Ω_{DG} starts with Ω_{BG}, but can be shut off prematurely, before the end of Δt_{catch}. A tomography measurement is performed after Δt_{catch}. **b, c**, Conditional tomography revealing the continuous, coherent and, surprisingly, deterministic flight (when completed) of the quantum jump from $|G\rangle$ to $|D\rangle$. The error bars are smaller than the size of the dots. The mid-flight time Δt_{mid} is defined by $Z_{\text{GD}} = 0$. The jump proceeds even when Ω_{DG} is turned off at the beginning of the flight (**c**), $\Delta t_{\text{on}} = 2\,\mu\text{s}$. Data obtained from 6.8×10^6 experimental realizations. Solid lines represent theoretical predictions (Supplementary Information section IIIA). Dashed lines in **c** are theoretical curves for the Δt_{on} interval, reproduced from **b**. The data suggest that an advance-warning signal of the jump can be provided by a no-click period for catch time $\Delta t_{\text{catch}} = \Delta t_{\text{mid}}$, at which half of the jumps will complete.

a modified formula (Supplementary Information section IIA3). The results demonstrate that the role of the Rabi drive Ω_{DG} is to initiate the jump and provide a reference for the phase of its evolution, complementing recent similar results in a different context[33]. Note that the $\Delta t_{\text{catch}} \gg \Delta t_{\text{mid}}$ non-zero steady-state value of X_{GD} in Fig. 3b is the result of the competition between the Rabi drive Ω_{DG} and the effect of the measurement of $|B\rangle$ (Supplementary Information section IIA2). This is confirmed in Fig. 3c, where $\Omega_{\text{DG}} = 0$, and where there is no offset in the steady-state value of X_{GD}.

The results of Fig. 3 demonstrate that despite the long-term unpredictability of the jumps from $|G\rangle$ to $|D\rangle$, they are preceded by an identical no-click record from run to run. Whereas the jump starts at a random time and can be prematurely interrupted by a click, the deterministic nature of the uninterrupted flight comes as a surprise given the quantum fluctuations in the heterodyne record I_{rec} during the jump—an island of predictability in a sea of uncertainty.
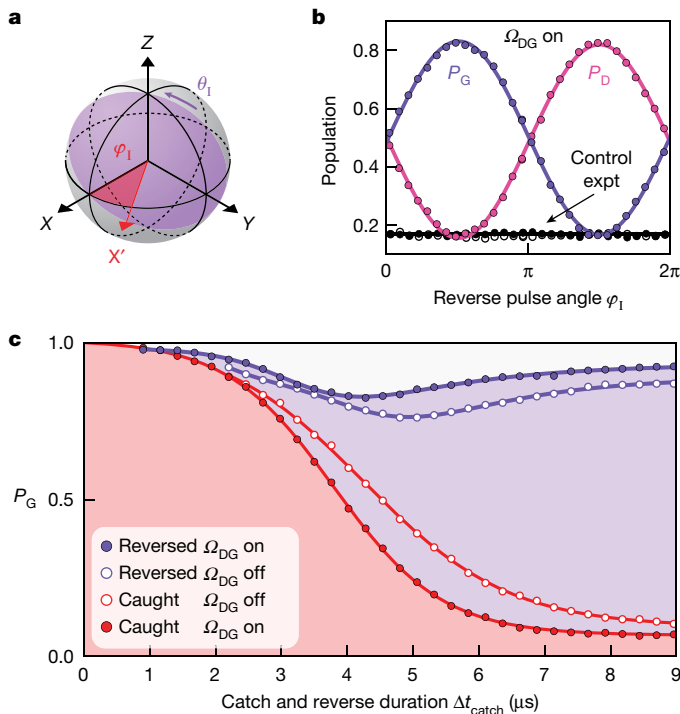
Fig. 4 | Reversing the quantum jump mid-flight. a, Bloch sphere of the GD manifold, showing the axis X' for the jump reversal, defined by the azimuthal angle φ_I. The angle of the intervention pulse is θ_I. **b**, Success probabilities P_G (purple) and P_D (orange) to reverse to $|G\rangle$ and complete to $|D\rangle$ the quantum jump mid-flight at $\Delta t_{catch} = \Delta t_{mid}$, with $\theta_I = \pi/2$, in the presence of the Rabi drive Ω_{DG}. The error bars are smaller than the size of the dots. Black dots show the success probability for $|G\rangle$ (closed dots) and $|D\rangle$ (open dots) in a control experiment in which intervention is applied at random times along the record, rather than at Δt_{catch}. **c**, Optimal success of reverse protocol (purple) as a function of Δt_{catch}. The FPGA controller is programmed with the optimal $\{\theta_I(\Delta t_{catch}), \varphi_I(\Delta t_{catch})\}$. Closed and open dots correspond to $\Delta t_{on} = \Delta t_{catch}$ and $\Delta t_{on} = 2\,\mu s$, respectively. Red points show the corresponding open-loop (no intervention) results from Fig. 3b, c.

In Fig. 4b, we show that by choosing $\Delta t_{catch} = \Delta t_{mid}$ for the no-click period to serve as an advance warning signal, we reverse the quantum jump in the presence of Ω_{DG}, confirming its coherence; the same result is found when Ω_{DG} is off (see Extended Data Fig. 3). The reverse pulse characteristics are defined in Fig. 4a. For $\varphi_I = \pi/2$, our feedback protocol succeeds in reversing the jump to $|G\rangle$ with 83.1% ± 0.3% fidelity, whereas for $\varphi_I = 3\pi/2$, the protocol completes the jump to $|D\rangle$, with 82.0% ± 0.3% fidelity. In a control experiment, we repeat the protocol by applying the reverse pulse at random times, rather than those determined by the advance warning signal. Without the advance warning signal, the measured populations only reflect those of the ensemble average.

In a final experiment, we programmed the controller with the optimal reverse pulse parameters $\{\theta_I(\Delta t_{catch}), \varphi_I(\Delta t_{catch})\}$, and as shown in Fig. 4c, we measured the success of the reverse protocol as a function of the catch time, Δt_{catch}. The filled/open dots indicate the results for Ω_{DG} on/off, and the solid curves are theory fits motivated by the exact analytic expressions (Supplementary Information section IIIA). The complementary red dots and curves reproduce the open-loop results of Fig. 3 for comparison.

From the experimental results of Fig. 2a one can infer, consistent with Bohr's initial intuition and the original ion experiments, that quantum jumps are random and discrete. Yet the results of Fig. 3 support a contrary view, consistent with that of Schrödinger: the evolution of the jump is coherent and continuous. The difference in timescales in the two figures allows the coexistence of these seemingly opposed point

of views and the reconciliation of the discreteness of countable events, such as jumps, with the continuity of the deterministic Schrödinger's equation. Furthermore, although all 6.8×10^6 recorded jumps (Fig. 3) are entirely independent of one another and stochastic in their initiation and termination, the tomographic measurements as a function of Δt_{catch} explicitly show that all jump evolutions follow an essentially identical, predetermined path in Hilbert space—not a randomly chosen one—and, in this sense, they are deterministic. These results are further corroborated by the reversal experiments shown in Fig. 4, which exploit the continuous, coherent, and deterministic nature of the jump evolution and critically hinge on prior knowledge of the Hilbert space path. With this knowledge ignored in the control experiment of Fig. 4b, failure of the reversal is observed.

In conclusion, these experiments, revealing the coherence of the jump, promote the view that a single quantum system under efficient, continuous observation is characterized by a time-dependent state vector inferred from the record of previous measurement outcomes, and whose meaning is that of an objective, generalized degree of freedom. The knowledge of the system on short timescales is not incompatible with unpredictable switching behaviour on long timescales. The excellent agreement between experiment and theory including known experimental imperfections (Supplementary Information section IIIA) thus provides support to the modern quantum trajectory theory and its reliability for predicting the performance of real-time intervention techniques in the control of single quantum systems.

Online content

Any methods, additional references, Nature Research reporting summaries, source data, statements of data availability and associated accession codes are available at https://doi.org/10.1038/s41586-019-1287-z.

1. Bohr, N. On the constitution of atoms and molecules. Part I. *Binding of electrons by positive nuclei. Phil. Mag.* **26**, 1–25 (1913).
2. Nagourney, W., Sandberg, J. & Dehmelt, H. Shelved optical electron amplifier: observation of quantum jumps. *Phys. Rev. Lett.* **56**, 2797–2799 (1986).
3. Sauter, T., Neuhauser, W., Blatt, R. & Toschek, P. E. Observation of quantum jumps. *Phys. Rev. Lett.* **57**, 1696 (1986).
4. Bergquist, J. C., Hulet, R. G., Itano, W. M. & Wineland, D. J. Observation of quantum jumps in a single atom. *Phys. Rev. Lett.* **57**, 1699–1702 (1986).
5. Carmichael, H. J. *An Open Systems Approach to Quantum Optics* (Springer, 1993).
6. Gardiner, C. W., Parkins, A. S. & Zoller, P. Wave-function quantum stochastic differential equations and quantum-jump simulation methods. *Phys. Rev. A* **46**, 4363–4381 (1992).
7. Dalibard, J., Castin, Y. & Mølmer, K. Wave-function approach to dissipative processes in quantum optics. *Phys. Rev. Lett.* **68**, 580–583 (1992).
8. Plenio, M. B. & Knight, P. L. The quantum-jump approach to dissipative dynamics in quantum optics. *Rev. Mod. Phys.* **70**, 101–144 (1998).
9. Korotkov, A. N. Continuous quantum measurement of a double dot. *Phys. Rev. B* **60**, 5737–5742 (1999).
10. Einstein, A. Strahlungs-emission und -absorption nach der Quantentheorie. *Verh. Deutsch. Phys. Ges.* **18**, 318–323 (1916).
11. Einstein, A. Quantentheorie der Strahlung. *Phys. Z.* **18**, 121–128 (1917).
12. Schrödinger, E. Are there quantum jumps? *Br. J. Phil. Sci.* **3**, 109–123; 233–242 (1952).
13. Basché, T., Kummer, S. & Bräuchle, C. Direct spectroscopic observation of quantum jumps of a single molecule. *Nature* **373**, 132–134 (1995).
14. Peil, S. & Gabrielse, G. Observing the quantum limit of an electron cyclotron: QND measurements of quantum jumps between Fock states. *Phys. Rev. Lett.* **83**, 1287–1290 (1999).
15. Gleyzes, S. S. et al. Quantum jumps of light recording the birth and death of a photon in a cavity. *Nature* **446**, 297–300 (2007).
16. Guerlin, C. et al. Progressive field-state collapse and quantum non-demolition photon counting. *Nature* **448**, 889–893 (2007).
17. Jelezko, F. et al. Single spin states in a defect center resolved by optical spectroscopy. *Appl. Phys. Lett.* **81**, 2160 (2002).
18. Neumann, P. et al. Single-shot readout of a single nuclear spin. *Science* **329**, 542–544 (2010).
19. Robledo, L. et al. High fidelity projective read-out of a solid-state spin quantum register. *Nature* **477**, 574–578 (2011).
20. Vijay, R., Slichter, D. H. & Siddiqi, I. Observation of quantum jumps in a superconducting artificial atom. *Phys. Rev. Lett.* **106**, 110502 (2011).
21. Hatridge, M. et al. Quantum back-action of an individual variable-strength measurement. *Science* **339**, 178–181 (2013).

22. Deléglise, S. et al. Reconstruction of non-classical cavity field states with snapshots of their decoherence. *Nature* **455**, 510–514 (2008).
23. Sayrin, C. et al. Real-time quantum feedback prepares and stabilizes photon number states. *Nature* **477**, 73–77 (2011).
24. Sun, L. et al. Tracking photon jumps with repeated quantum non-demolition parity measurements. *Nature* **511**, 444–448 (2014).
25. Ofek, N. et al. Demonstrating quantum error correction that extends the lifetime of quantum information. *Nature* **536**, 441–445 (2016).
26. Porrati, M. & Putterman, S. Wave-function collapse due to null measurements: the origin of intermittent atomic fluorescence. *Phys. Rev. A* **36**, 929–932 (1987).
27. Mabuchi, H. & Zoller, P. Inversion of quantum jumps in quantum optical systems under continuous observation. *Phys. Rev. Lett.* **76**, 3108–3111 (1996).
28. Ruskov, R., Mizel, A. & Korotkov, A. N. Crossover of phase qubit dynamics in the presence of a negative-result weak measurement. *Phys. Rev. B* **75**, 220501 (2007).
29. Volz, J., Gehr, R., Dubois, G., Esteve, J. & Reichel, J. Measurement of the internal state of a single atom without energy exchange. *Nature* **475**, 210–213 (2011).
30. Ristè, D. et al. Deterministic entanglement of superconducting qubits by parity measurement and feedback. *Nature* **502**, 350–354 (2013).
31. Murch, K. W., Weber, S. J., Beck, K. M., Ginossar, E. & Siddiqi, I. Reduction of the radiative decay of atomic coherence in squeezed vacuum. *Nature* **499**, 62–65 (2013).
32. Weber, S. J. et al. Mapping the optimal route between two quantum states. *Nature* **511**, 570–573 (2014).
33. Katz, N. et al. Coherent state evolution in a superconducting qubit from partial-collapse measurement. *Science* **312**, 1498–1500 (2006).

Author contributions Z.K.M. initiated, designed and performed the experiment, designed the sample, analysed the data and carried out the initial theoretical and numerical modelling of the experiment. Z.K.M. conceived the experiment based on theoretical predictions by H.J.C. H.J.C. and R.G.-J. performed the presented theoretical modelling and numerical simulations. S.O.M. contributed to the experimental set-up and design of the device. S.O.M. and S.S. contributed to the fabrication of the device. P.R. and R.J.S. assisted with the FPGA. M.M. contributed theoretical support. M.H.D. supervised the project. Z.K.M. and M.H.D. wrote the manuscript. H.J.C. contributed the theoretical supplement. All authors provided suggestions for the experiment, discussed the results and contributed to the manuscript.

Competing interests R.J.S. and M.H.D. are founders, and R.J.S. is an equity shareholder, of Quantum Circuits, Inc.

Additional information
Extended data is available for this paper at https://doi.org/10.1038/s41586-019-1287-z.
Supplementary information is available for this paper at https://doi.org/10.1038/s41586-019-1287-z.
Reprints and permissions information is available at http://www.nature.com/reprints.
Correspondence and requests for materials should be addressed to Z.M. or M.D.
Publisher's note: Springer Nature remains neutral with regard to jurisdictional claims in published maps and institutional affiliations.

METHODS

Monitoring quantum jumps. Here, we explain briefly how the GD dynamics is monitored and when we conclude that a quantum jump has occurred.

Monitoring the GD manifold through B de-excitations. The state of the atom within the GD manifold is monitored indirectly, by measuring the rate of de-excitations from the ancillary state $|B\rangle$, while the G to B excitation tone Ω_{BG} is applied. As explained below, the monitoring scheme is such that when the atom is in the dark state, $|D\rangle$, the rate of de-excitations from $|B\rangle$ to $|G\rangle$ is zero. Conversely, when the atom is in $|G\rangle$, the rate is non-zero. Henceforth, we will refer to a de-excitation from $|B\rangle$ to $|G\rangle$ simply as a de-excitation. In summary, when the rate of de-excitations for a measurement segment is zero, $|D\rangle$ is assigned to it; otherwise, $|G\rangle$ or $|B\rangle$ is assigned (see 'IQ filter' section of Methods). The rate can be monitored by either a direct or an indirect method, as explained further below.

Quantum jumps. Sections of the (continuous) measurement record are converted into state assignments, as discussed above, such as B, G or D. In the experiment, long sequences of such measurements yield the same result, that is, GGG… or DDD… When the string of results suddenly switches its value, we say that a quantum jump has occurred[34].

Source of the difference for the de-excitation rates. The rate of de-excitations is zero when the atom is in $|D\rangle$ because the V-shaped level structure forbids any direct DB transitions; hence, $|B\rangle$ cannot be excited from $|D\rangle$. Conversely, when the atom is in $|G\rangle$, the Rabi drive Ω_{BG} can excite the atom to $|B\rangle$. Because this ancillary state is effectively short-lived, it almost immediately de-excites back to $|G\rangle$. Note that in this explanation we neglect parasitic transitions to higher excited states, which are considered in the Supplement.

Direct or indirect de-excitation detection. A de-excitation can be detected by a direct or, alternatively, indirect method. For atomic experiments, direct detection is a natural choice. The photon emitted by the atom during the de-excitation, carrying away the energy once stored in $|B\rangle$, is collected and destructively absorbed in the sensor of a photodetecting measurement apparatus, which produces a click signal (in practice, a current or voltage pulse). Unfortunately, unavoidable imperfections and detector non-idealities prohibit this method for the continuous detection of nearly every single de-excitation (Supplementary Information section III). Alternatively, one can use an indirect monitoring method. In our experiment, instead of detecting the emitted photon, we detect the de-excitation by monitoring the $|B\rangle$ population through an ancillary degree of freedom, the readout cavity, coupled to the atom.

Indirect (dispersive) detection. The readout cavity frequency depends on the state of the atom. When the atom is in $|B\rangle$, the readout cavity frequency shifts down by more than a cavity linewidth. The cavity frequency, and hence the $|B\rangle$ population of the atom, is probed by a continuous readout tone applied at the $|B\rangle$-cavity frequency. When the atom is in $|B\rangle$, the probe tone is resonant and fills the cavity with a large number of photons, $\bar{n}$. Otherwise, when the atom is not-in-$|B\rangle$, the probe tone is far off resonant and the cavity is empty of photons. Choosing $\bar{n} \gg 1$ makes a change in the $|B\rangle$ occupancy conspicuous, and hence a de-excitation, $|B\rangle$ to not-$|B\rangle$, is readily observed, even in the presence of measurement inefficiencies and imperfections. As explained in Supplementary Information section IIIC, this indirect dispersive method in effect increases the signal-to-noise ratio and de-excitation detection efficiency. Another notable difference between the direct and indirect method is that in the indirect method the atom fully but briefly occupies $|B\rangle$ before de-exciting to $|G\rangle$, whereas in the direct scheme the probability amplitude to be in $|B\rangle$ is never appreciable before a de-excitation (see Supplementary Information section II). In other words, in the direct monitoring scheme, there are explicitly two sets of quantum jumps: the BG and DG ones. The BG ones occurs much faster and are nested within the DG jumps. The fast dynamics of these 'inner' jumps is used to interrogate the dynamics of 'outer' DG jumps.

Set-up of the experiment. Our experiments were carried out in a cryogen-free dilution refrigerator (Oxford Triton 200). The cavity and Josephson parametric converter[35] were shielded from stray magnetic fields by a cryogenic μ-metal (Amumetal A4K) shield. Our input–output cryogenic set-up is nearly identical to that described in ref. [25], aside from the differences evident in the schematic of our set-up (see Fig. 1b and Methods) or described in the following.

The control tones depicted in Fig. 1 were each generated from individual microwave generators (Ω_{DG} and Ω_{B0}: Agilent N5183A; readout cavity tone R and Ω_{B1}: Vaunix LabBrick LMS-103-13 and LMS-802-13, respectively). To achieve IQ control, the generated tones were mixed (Marki Microwave Mixers IQ-0618LXP for the cavity and IQ-0307LXP for Ω_{B0}, Ω_{B1} and Ω_{DG}) with intermediate-frequency signals synthesized by the 16-bit digital-to-analogue converters of the integrated FPGA controller system (Innovative Integration VPXI-ePC). Before mixing, each analogue output was filtered by a 50 Ω low-pass filter (Mini-Circuits BLP-300+) and attenuated by a minimum of 10 dB. The radio-frequency output was amplified at room temperature (MiniCircuits ZVA-183-S+) and filtered by Mini-Circuits coaxial bandpass filters. The output signal was further pulse-modulated by the FPGA with high-isolation single-pole, single-throw (SPST) switches (Analog

Devices HMC-C019), which provided additional 80 dB isolation when the control drives were turned off. The signals were subsequently routed to the input lines of the refrigerator, whose details were described in refs [25,36].

At room temperature, following the cryogenic high-electron-mobility amplifier (Low Noise Factory LNF-LNC7_10A), the signals were amplified by 28 dB (Miteq AFS3-00101200-35-ULN) before being mixed down (Marki image reject double-balanced mixer IRW-0618) to an intermediate frequency of 50 MHz, where they were band-pass filtered (Mini-Circuits SIF-50+) by and further amplified by a cascaded preamplifier (Stanford Research Systems SR445A), before final digitization by the FPGA analogue-to-digital converters.

Atom-cavity implementation. The superconducting artificial atom consisted of two coupled transmon qubits fabricated on a 2.9 mm × 7 mm, double-side-polished, *c*-plane sapphire wafer with the Al/AlO$_x$/Al bridge-free electron-beam lithography technique[37,38]. The first transmon (B) was aligned with the electric field of the fundamental TE$_{101}$ mode of an aluminium rectangular cavity (alloy 6061; dimensions: 5.08 mm by 35.5 mm × 17.8 mm), while the second transmon (D) was oriented perpendicular to the first and positioned 170 μm adjacent to it. The inductance of the Josephson junction of each transmon (9 nH for both B and D), the placement and dimensions of each transmon, and the geometry of the cavity were designed and optimized using finite-element electromagnetic analysis and the energy-participation-ratio method[39]. The analysis also verified that the coupling between the two qubits is described by the Hamiltonian $\hat{H}_{int} = -\chi_{DB}\hat{n}_B \otimes \hat{n}_D$, where $\hat{n}_{B/D}$ is the photon number operator of the B/D qubit, and χ_{DB} is the cross-Kerr frequency.

The measured frequency and anharmonicity of the D qubit were $\omega_D/2\pi = 4845.255$ MHz and $\alpha_{DG}/2\pi = 152$ MHz, respectively, while those of the B qubit were $\omega_B/2\pi = 5570.349$ MHz and $\alpha_{BG}/2\pi = 195$ MHz, respectively. The cross-Kerr coupling was $\chi_{DB}/2\pi = 61$ MHz. The relaxation time of $|B\rangle$ was $T_1^B = 28 \pm 2$ μs, limited by the Purcell effect by design, and its Ramsey coherence time was $T_{2R}^B = 18 \pm 1$ μs. The remaining parameters of the system are provided in the main text.

Atom and cavity drives. In all experiments, the following drive parameters were used. The DG Rabi drive, Ω_{DG}, was applied 275 kHz below ω_D, to account for the Stark shift of the cavity. The BG drive, Ω_{BG}, was realized as a bichromatic tone to unselectively address the BG transition, which was broadened and Stark-shifted owing to the coupling between $|B\rangle$ and the readout cavity. Specifically, we address transitions from $|G\rangle$ to $|B\rangle$ with a Rabi drive $\Omega_{B0}/2\pi = 1.20 \pm 0.01$ MHz at frequency ω_{BG}, whereas transitions from $|B\rangle$ to $|G\rangle$ are addressed with a Rabi drive $\Omega_{B1}/2\pi = 0.60 \pm 0.01$ MHz tuned 30 MHz below ω_{BG}. This bichromatic scheme provided the ability to tune the up-click and down-click rates independently, but otherwise essentially functioned as an incoherent broadband source.

IQ filter. To mitigate the effects of imperfections in the atom readout scheme in extracting a $|B\rangle$/not-$|B\rangle$ result, we applied a two-point, hysteretic IQ filter, implemented on the FPGA controller in real time. The filter is realized by comparing the present quadrature record values $\{I_{rec}, Q_{rec}\}$, with three thresholds (I_B, $I_{\bar{B}}$ and Q_B) as summarized in Extended Data Table 1.

The filter and thresholds were selected to provide a best estimate of the time of a click, operationally understood as a change in the filter output from $|B\rangle$ to not-$|B\rangle$. The I_B and $I_{\bar{B}}$ thresholds were chosen 1.5 standard deviations away from the *I*-quadrature mean of the $|B\rangle$ and not-$|B\rangle$ distributions, respectively. The Q_B threshold was chosen three standard deviations away from the *Q*-quadrature mean. Higher excited states of the atom were selected out by Q_{rec} values exceeding the Q_B threshold.

Tomography. At the end of each experimental realization, we performed one of 15 rotation sequences on the atom that transferred information about one component of the density matrix, $\hat{\rho}_a$, to the population of $|B\rangle$, which was measured with a 600-ns square pulse on the readout cavity. Pulses were calibrated with a combination of Rabi, derivative removal via adiabatic gate[40], All-XY[41] and amplitude pulse-train sequences[42]. The readout signal was demodulated with the appropriate digital filter function required to realize temporal mode matching[43]. To remove the effect of potential systematic offset errors in the readout signal, we subtracted the measurement results of operator components of $\hat{\rho}_a$ and their opposites. From the measurement results of this protocol, we reconstructed the density matrix $\hat{\rho}_a$ and subsequently parametrized it in the useful form

$$\hat{\rho}_a = \begin{pmatrix} \dfrac{N}{2}(1-Z_{GD}) & \dfrac{N}{2}(X_{GD}+iY_{GD}) & R_{BG}+iI_{BG} \\[2ex] \dfrac{N}{2}(X_{GD}-iY_{GD}) & \dfrac{N}{2}(1+Z_{GD}) & R_{BD}+iI_{BD} \\[2ex] R_{BG}-iI_{BG} & R_{BD}-iI_{BD} & 1-N \end{pmatrix}$$

where X_{GD}, Y_{GD} and Z_{GD} are the Bloch vector components of the GD manifold, N is the total population of the $|G\rangle$ and $|D\rangle$ states, while R_{BG}, R_{BD}, I_{BG} and I_{BD} are the coherences associated with $|B\rangle$, relative to the GD manifold. The measured

population in $|B\rangle$, $1 - N$, remains below 0.03 during the quantum jump (see Extended Data Fig. 3). Tomographic reconstruction was calibrated and verified by preparing Clifford states, accounting for the readout fidelity of 97%.

Control flow of the experiment. A diagrammatic representation of the control flow of the experiment is illustrated in Extended Data Fig. 4a, whose elements are briefly described in the following.

'Start': FPGA controller resets its internal memory registers to zero[25,44], including the no-click counter 'cnt', defined below. 'Prepare B': controller deterministically prepares the atom in $|B\rangle$, a maximally conservative initial state, with measurement-based feedback[45]. 'Initialize': controller turns on the atom (Ω_{BG} and Ω_{DG}) and cavity (R) drives and begins demodulation. 'Monitor and catch Δt_{on}': with all drives on (Ω_{BG}, Ω_{DG} and R), the controller actively monitors the cavity output signal until it detects no-clicks for duration Δt_{on}, as described in Extended Data Fig. 4b, whereafter the controller proceeds to 'monitor and catch Δt_{off}' in the case that $\Delta t_{off} > 0$; otherwise, for $\Delta t_{off} = 0$, the controller proceeds to 'tomography' ('feedback pulse') for the catch (reverse) protocol. 'Monitor and catch Δt_{off}': with the Rabi drive Ω_{DG} off, while keeping the drives Ω_{BG} and R on, the controller continues to monitor the output signal. The controller exits the routine only in one of two events: (i) if it detects a click, in which case it proceeds to the 'declare B' step of the monitor and catch Δt_{on} routine, or (ii) if no further clicks are detected for the entirety of the pre-defined duration Δt_{off}, in which case the controller advances to the tomography (feedback pulse) routine, when programmed for the catch (reverse) protocol. 'Feedback pulse': with all continuous-wave drives turned off, the controller performs a pulse on the DG transition of the atom, defined by the two angles $\{\theta_I(\Delta t_{catch}), \varphi_I(\Delta t_{catch})\}$. 'Tomography': controller performs next-in-order tomography sequence (see Tomography section above) while the demodulator finishes processing the final data in its pipeline. 'Advance tomo.': tomography sequence counter is incremented; after a 50-µs delay, the next realization of the experiment is started.

The concurrent-programming control flow of the 'monitor and catch Δt_{on}' block is illustrated in Extended Data Fig. 4b; specifically, the master and demodulator modules of the controller and synchronous sharing of data between them is depicted. The FPGA demodulator outputs a pair of 16-bit signed integers, $\{I_{rec}, Q_{rec}\}$, every $T_{int} = 260$ ns, which is routed to the master module, as depicted by the large left-pointing arrow (top). The master module implements the IQ filter (see 'IQ filter' section above) and tracks the number of consecutive not-$|B\rangle$ measurement results with the counter cnt. The counter thus keeps track of the no-click time elapsed since the last click, which is understood as a change in the measurement result from $|B\rangle$ to not-$|B\rangle$. When the counter reaches the critical value N_{on}, corresponding to Δt_{on}, the master and demodulator modules synchronously exit the current routine: see the T∗ branch of the 'declare not-B' decision block. Until this condition is fulfilled (F∗), the two modules proceed within the current routine as depicted by the black flowlines. To minimize latency and maximize computation throughput, the master and demodulator were designed to be independent sequential processes running concurrently on the FPGA controller, communicating strictly through synchronous message passing, which imposed stringent synchronization and execution time constraints. All master intermodule logic was constrained to run at a 260-ns cycle, the start of which necessarily was imposed to coincide with a 'receive and stream record' operation, here denoted by the stopwatch. In other words, this imposed the algorithmic constraint that all flowchart paths starting at a stopwatch and ending at a stopwatch were constrained to a 260-ns execution timing. A second key timing constraint was imposed by the time required to propagate signals between the different FPGA cards, which corresponded to a minimum branching-instruction duration of 76 ns.

The corresponding demodulation-module flowchart is identical to that shown in Extended Data Fig. 4b; hence, it is not shown. This routine functions in the following manner: if a $|B\rangle$ outcome is detected, the controller jumps to the 'declare B' block of the monitor and catch Δt_{on} routine; otherwise, when only not-$|B\rangle$ outcomes are observed, and the counter reaches the critical value N_{off}, corresponding to $\Delta t_{catch} = \Delta t_{on} + \Delta t_{off}$, the controller exits the routine.

Data availability

The data that support the findings of this study are available from the corresponding authors on reasonable request.

34. Cook, R. J. What are quantum jumps? *Phys. Scr.* **1988**, 49 (1988).
35. Bergeal, N. et al. Phase-preserving amplification near the quantum limit with a Josephson ring modulator. *Nature* **465**, 64–68 (2010).
36. Minev, Z. et al. Planar multilayer circuit quantum electrodynamics. *Phys. Rev. Appl.* **5**, 044021 (2016).
37. Lecocq, F. et al. Junction fabrication by shadow evaporation without a suspended bridge. *Nanotechnology* **22**, 315302 (2011).
38. Rigetti, C. T. *Quantum Gates for Superconducting Qubits*. PhD thesis, Yale Univ. (2009).
39. Minev, Z. K. *Catching and Reversing a Quantum Jump Mid-Flight*. PhD thesis, Yale Univ. (2019).
40. Chow, J. M. et al. Optimized driving of superconducting artificial atoms for improved single-qubit gates. *Phys. Rev. A* **82**, 040305 (2010).
41. Reed, M. D. *Entanglement and Quantum Error Correction with Superconducting Qubits*. PhD thesis, Yale Univ. (2013).
42. Bylander, J. et al. Noise spectroscopy through dynamical decoupling with a superconducting flux qubit. *Nat. Phys.* **7**, 565–570 (2011).
43. Eichler, C. et al. Observation of entanglement between itinerant microwave photons and a superconducting qubit. *Phys. Rev. Lett.* **109**, 240501 (2012).
44. Liu, Y. *Quantum Feedback Control of Multiple Superconducting Qubits*. PhD thesis, Yale Univ. (2016).
45. Ristè, D., Bultink, C. C., Lehnert, K. W. & DiCarlo, L. Feedback control of a solid-state qubit using high-fidelity projective measurement. *Phys. Rev. Lett.* **109**, 240502 (2012).
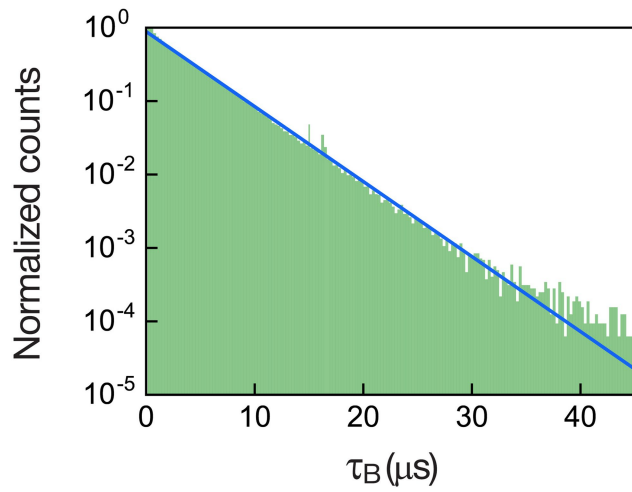
Extended Data Fig. 1 | Waiting time to switch from a |B⟩ to not-|B⟩ state assignment result. Semi-log plot of the histogram (shaded green) of the duration of times corresponding to |B⟩-measurement results, τ_B, for 3.2 s of continuous data of the type shown in Fig. 2a. Solid line is an exponential fit which yields a 4.2 ± 0.03 μs time constant.

a

Re $\rho_c(\Delta t_{mid})$

b

Im $\rho_c(\Delta t_{mid})$
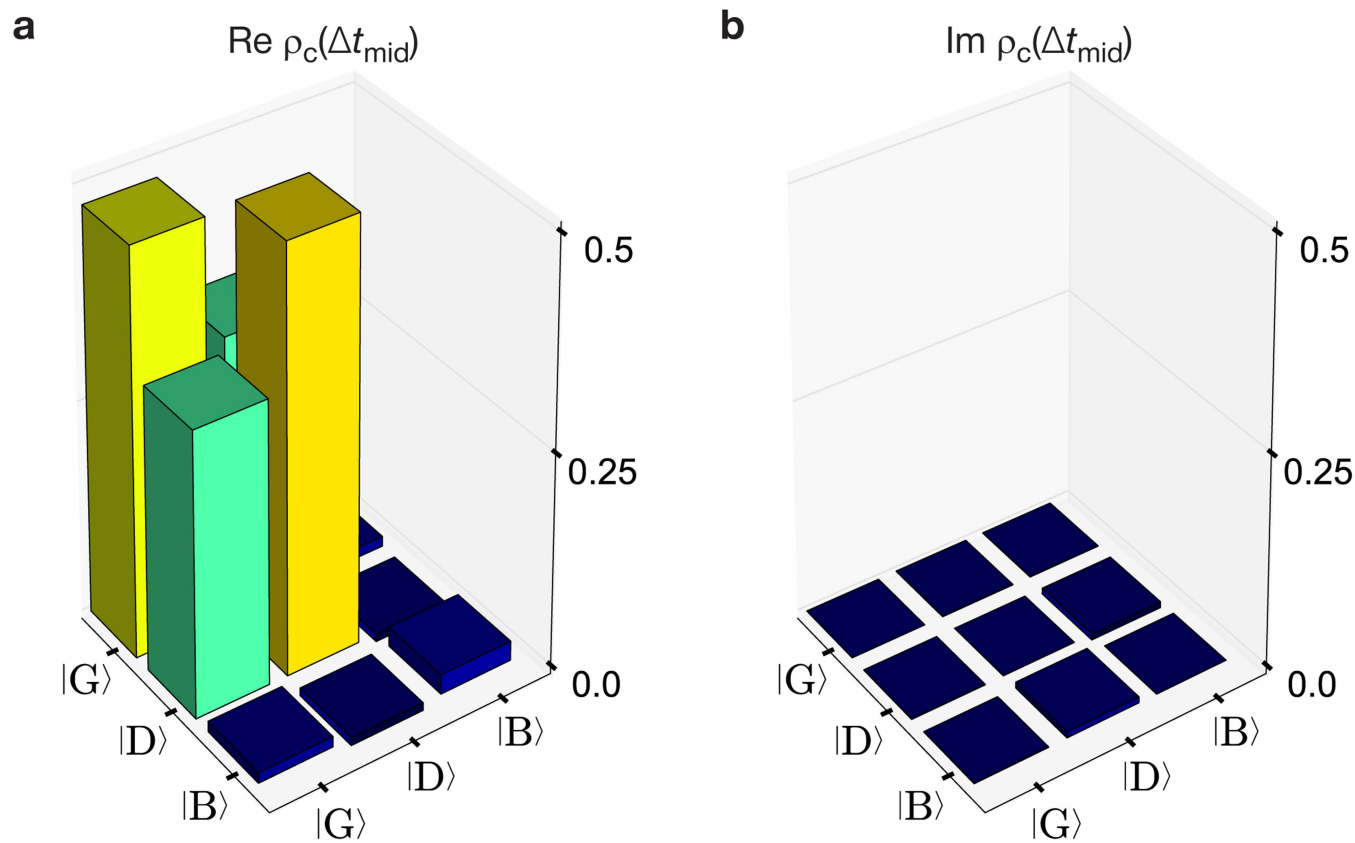
Extended Data Fig. 2 | Mid-flight tomogram. a, **b**, The plots show the real (**a**) and imaginary (**b**) parts of the conditional density matrix, ρ_c, at the mid-flight of the quantum jump ($\Delta t_{catch} = \Delta t_{mid}$), in the presence of the Rabi drive from $|G\rangle$ to $|D\rangle$ ($\Delta t_{off} = 0$). The population of the $|B\rangle$ state is 0.023, and the magnitude of all imaginary components is less than 0.007.
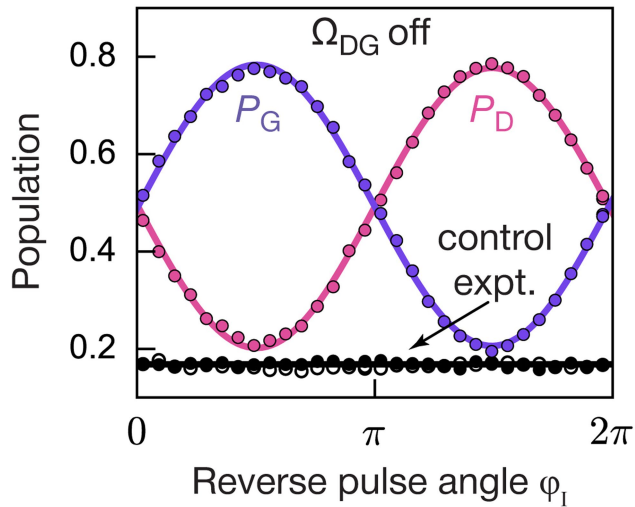
Extended Data Fig. 3 | Reversing the quantum jump mid-flight in the absence of Ω_{DG}. Success probabilities P_G (purple) and P_D (orange) to reverse to $|G\rangle$ and complete to $|D\rangle$ the quantum jump mid-flight at $\Delta t_{catch} = \Delta t'_{mid}$, defined in Fig. 3b, in the absence of the Rabi drive Ω_{DG}, where $\Delta t_{on} = 2\,\mu s$ and $\theta_I = \pi/2$. The error bars are smaller than the size of the dots. In the presence of Ω_{DG}, P_G is 5% larger owing to a smaller T_2 effect. Black dots denote the success probability for $|G\rangle$ (closed dots) and $|D\rangle$ (open dots) for the control experiment in which the intervention is applied at random times (see Fig. 4b).
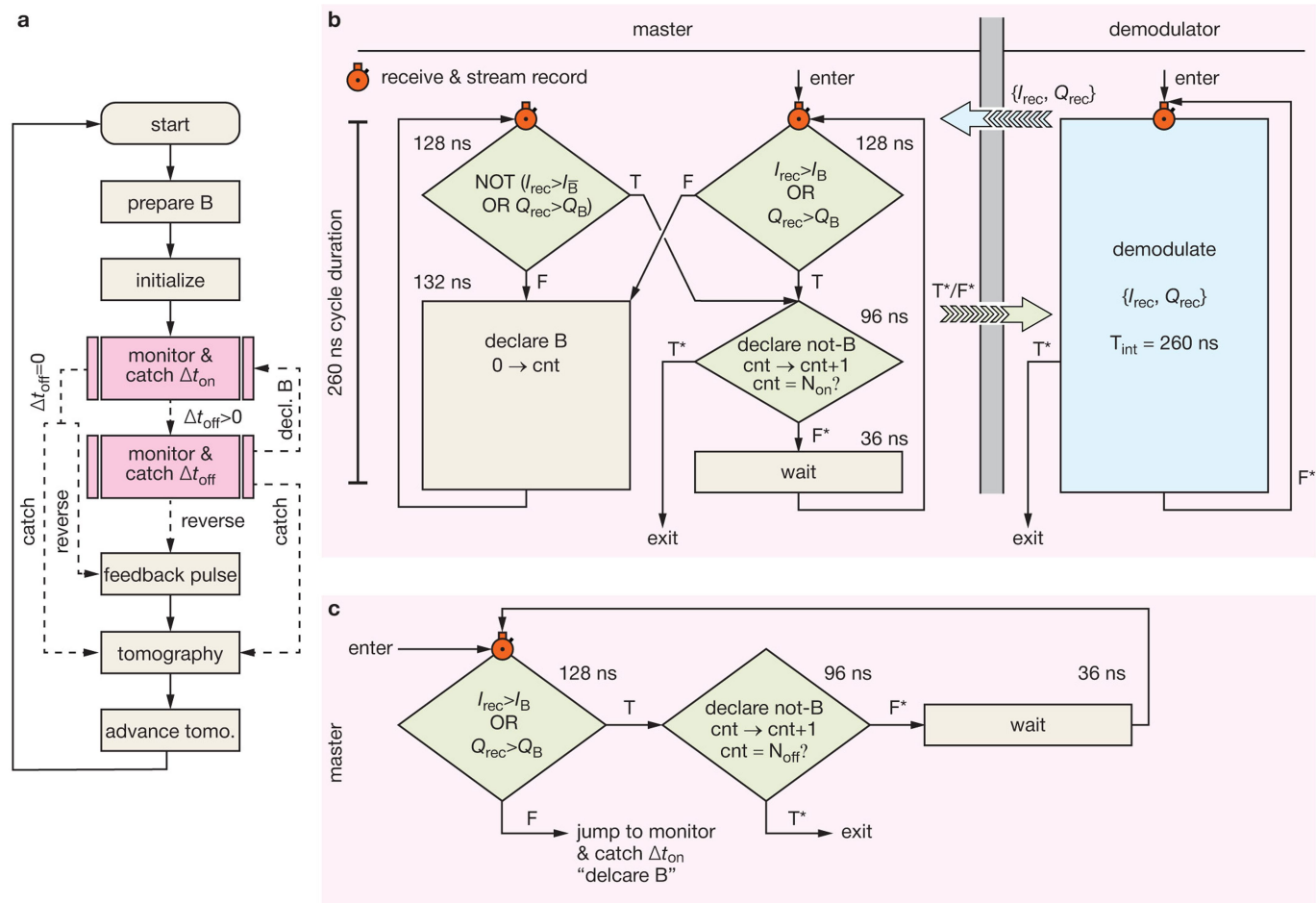
Extended Data Fig. 4 | Control flow of the experiment. a, Flowchart illustrating the control flow of the catch and reverse experiments, whose results are shown in Figs. 3, 4. See Methods for the description of each block. **b**, Flowchart of the master and demodulator modules chiefly involved in the 'monitor and catch Δt_{on}' routine. The modules execute concurrently and share data synchronously, as discussed in Methods. **c**, Flowchart of the processing involved in the master module of the 'monitor and catch Δt_{off}' routine; see Methods.

Extended Data Table 1 | Input–output table summarizing the behaviour of the IQ filter implemented on the FPGA controller

Input:	$Q_{\mathrm{rec}} \geq Q_{\mathrm{B}}$ or $I_{\mathrm{rec}} > I_{\mathrm{B}}$	$Q_{\mathrm{rec}} < Q_{\mathrm{B}}$ and $I_{\mathrm{rec}} < I_{\bar{\mathrm{B}}}$	$Q_{\mathrm{rec}} < Q_{\mathrm{B}}$ and $I_{\bar{\mathrm{B}}} \leq I_{\mathrm{rec}} \leq I_{\mathrm{B}}$
Output:	$|\mathrm{B}\rangle$	not-$|\mathrm{B}\rangle$	previous

Extended Data Table 2 | Summary of timescales

Symbol	Value	Description
Γ^{-1}	$\approx 8.8\,\mathrm{ns}$	Effective measurement time of $|\mathrm{B}\rangle$, approximately given by $1/\kappa\bar{n}$, where $\bar{n} = 5 \pm 0.2$ in the main experiment (see Supplement Sec. II)
κ^{-1}	$44.0 \pm 0.06\,\mathrm{ns}$	Readout cavity lifetime
T_{int}	$260.0\,\mathrm{ns}$	Integration time of the measurement record, set in the controller at the beginning of the experiment
$\Gamma_{\mathrm{BG}}^{-1}$	$0.99 \pm 0.06\,\mathrm{\mu s}$	Average time the atom rests in $|\mathrm{G}\rangle$ before an excitation to $|\mathrm{B}\rangle$, see Fig. 2b
Δt_{mid}	$3.95\,\mathrm{\mu s}$	No-click duration for reaching $Z_{\mathrm{GD}} = 0$ in the flight of the quantum jump from $|\mathrm{G}\rangle$ to $|\mathrm{D}\rangle$, in the full presence of Ω_{DG}, see Fig. 3b
$\Gamma_{\mathrm{GD}}^{-1}$	$30.8 \pm 0.4\,\mathrm{\mu s}$	Average time the atom stays in $|\mathrm{D}\rangle$ before returning to $|\mathrm{G}\rangle$ and being detected, see Fig. 2b
T_1^{D}	$116 \pm 5\,\mathrm{\mu s}$	Energy relaxation time of $|\mathrm{D}\rangle$
$T_{2\mathrm{R}}^{\mathrm{D}}$	$120 \pm 5\,\mathrm{\mu s}$	Ramsey coherence time of $|\mathrm{D}\rangle$
$T_{2\mathrm{E}}^{\mathrm{D}}$	$162 \pm 6\,\mathrm{\mu s}$	Echo coherence time of $|\mathrm{D}\rangle$
$\Gamma_{\mathrm{DG}}^{-1}$	$220 \pm 5\,\mathrm{\mu s}$	Average time between two consecutive $|\mathrm{G}\rangle$ to $|\mathrm{D}\rangle$ jumps

List of the characteristic timescales involved in the catch and reverse experiment. The Hamiltonian parameters of the system are summarized in Supplementary Information section 1.